

The mixing transition in Rayleigh–Taylor instability

By ANDREW W. COOK, WILLIAM CABOT
AND PAUL L. MILLER

Lawrence Livermore National Laboratory, Livermore, CA 94550, USA

(Received 22 September 2003 and in revised form 5 March 2004)

A large-eddy simulation technique is described for computing Rayleigh–Taylor instability. The method is based on high-wavenumber-preserving subgrid-scale models, combined with high-resolution numerical methods. The technique is verified to match linear stability theory and validated against direct numerical simulation data. The method is used to simulate Rayleigh–Taylor instability at a grid resolution of 1152^3 . The growth rate is found to depend on the mixing rate. A mixing transition is observed in the flow, during which an inertial range begins to form in the velocity spectrum and the rate of growth of the mixing zone is temporarily reduced. By measuring growth of the layer in units of dominant initial wavelength, criteria are established for reaching the hypothetical self-similar state of the mixing layer. A relation is obtained between the rate of growth of the mixing layer and the net mass flux through the plane associated with the initial location of the interface. A mix-dependent Atwood number is defined, which correlates well with the entrainment rate, suggesting that internal mixing reduces the layer's growth rate.

1. Introduction

Rayleigh–Taylor instability (RTI) is the baroclinic generation of vorticity at a perturbed interface subject to acceleration in a direction opposite the mean density gradient (Rayleigh 1883; Taylor 1950; Chandrasekhar 1955). The resulting interpenetration and mixing of materials has far-reaching consequences in many natural and man-made flows, ranging from supernovae to inertial confinement fusion (ICF). In supernovae, the rate of growth of the mixing region is thought to be a controlling factor in the rate of formation of heavy elements. In ICF, accurate prediction of the depth of interpenetration of the fluids is crucial in designing capsules to maintain shell integrity. Because of the widespread importance of RTI, much attention over the past half century has been focused on predicting its late-time growth rate.

At sufficiently late times, the extent of the mixing region has historically been assumed to follow $\alpha A g t^2$ (Anuchina *et al.* 1978; Youngs 1984), where α is a dimensionless coefficient, $A \equiv (\rho_2 - \rho_1)/(\rho_2 + \rho_1)$ is the Atwood number (with ρ_1 and ρ_2 being the densities of the light and heavy fluids, respectively), g is the acceleration and t is time. This similarity solution results from dimensional analysis if the following conditions are met: (I) all memory of initial conditions is lost, (II) there are no boundary effects, and (III) viscosity and diffusivity (or surface tension) are not important. Satisfying all three of these requirements has proved extremely difficult, both experimentally and computationally.

Regarding (I), there is some current debate as to whether initial conditions can ever be completely forgotten (Cook & Dimotakis 2001; Clark 2003). Nevertheless, there is broad consensus that initial conditions are felt at least until the mixing layer grows large compared to the longest wavelength present in the initial perturbations (Glimm *et al.* 2001; Dimonte *et al.* 2004). Hence, the best hope for observing self-similar growth is to seed the perturbations at the smallest possible scales. In a numerical simulation, the minimum perturbation wavelength is limited by the grid spacing, Δ , and the resolving power of the differencing scheme. Regarding (II), the ‘bubble merger’ process is halted when the dominant wavelength, λ , or ‘bubble diameter’ grows close to the domain width, L . Additionally, as the number of modes in the domain (L/λ) decreases, statistical measures of the mixing width become less reliable. Hence, it is desirable to make L as large as possible in both experiments and simulations. Regarding (III), effects of diffusive processes on the growth rate can only be neglected if they occur on scales far smaller than λ , i.e. the bubble diameter must be much larger than both the Kolmogorov and Batchelor scales. This requires that the Reynolds number and Schmidt number both be large enough to allow significant power-law ranges to develop in the velocity and density spectra. Finally, if the mixing rate is determined by the large-scale entrainment rate, and not the diffusion scale where molecular mixing actually occurs, then effects of miscibility cannot be neglected at any Reynolds number. Indeed, Youngs (1991) has noted that experiments using immiscible fluids (Read 1984), though conducted at high Reynolds number, may have overestimated the value of α for miscible fluids.

Experiments enjoy a significant advantage over numerical simulations when it comes to achieving high Reynolds number. However, it is much easier to control initial perturbations in a simulation than it is in an experiment. Experiments involving accelerated tanks (Read 1984; Dimonte & Schneider 2000) typically have uncharacterized initial perturbations and experiments involving retracting plates (Duff, Harlow & Hirt 1962; Dalziel, Linden & Youngs 1999) are known to introduce unwanted large-scale disturbances into the flow. In order to observe the flow in the pure ‘mode coupling’ limit, it is necessary that no significant energy be initially present in low and moderate wavenumber. Thus, simulations appear to provide the best hope for reaching the hypothetical self-similar state, at least until experiments can be designed with well-characterized fine-scale initial perturbations.

The ideal numerical simulation would consist of an exponentially accurate (spectral) solution to the full Navier–Stokes equations, where all scales of motion, including the Kolmogorov and Batchelor scales, are fully resolved. Such is the goal of direct numerical simulation (DNS). DNS however, is severely restricted in the range of Reynolds numbers and Schmidt numbers of flows it can represent. Cook & Zhou (2002) performed DNS of RTI using 535 million grid points, however, their final Reynolds number (5500) was insufficient to support a significant inertial range in the energy spectrum of the density field. With large-eddy simulation (LES), wherein only the large growth-controlling scales of motion are resolved, it is possible to satisfy all three of the listed requirements; such is the goal of this work.

The layout of this paper is as follows. In § 2, the governing equations and LES solution technique are presented for an incompressible RTI flow. An incompressible formulation is chosen so that the fluids on either side of the interface can be initialized with constant density, and to eliminate sound waves as a constraint on the time step. In § 3, various flow quantities are defined for the purpose of modelling and analysis. In § 4, several verification and validation tests of the LES method are performed. In § 5, initial conditions and simulation details are described for the RTI flow under

investigation. In § 6, various results are presented from the LES. In § 7, a relation is derived between the rate of growth of the mixing layer and the net mass flux through the mid-plane. Finally, in § 8, conclusions are drawn regarding the effects of mixing on the flow and some speculations are made concerning the asymptotic state of growth.

2. Governing equations

2.1. Conservation laws

The governing equations for flows comprised of two incompressible miscible fluids in an accelerated Cartesian frame of reference are

$$\frac{\partial \rho Y_m}{\partial t} + \frac{\partial \rho Y_m u_j}{\partial x_j} = \frac{\partial}{\partial x_j} \left(\rho D \frac{\partial Y_m}{\partial x_j} \right) \quad (m = 1, 2), \quad (2.1)$$

$$\frac{\partial \rho u_i}{\partial t} + \frac{\partial \rho u_i u_j}{\partial x_j} = -\frac{\partial p}{\partial x_i} + \frac{\partial \tau_{ij}}{\partial x_j} + \rho g_i, \quad (2.2)$$

where

$$\tau_{ij} = \mu \left[\frac{\partial u_i}{\partial x_j} + \frac{\partial u_j}{\partial x_i} - \frac{2}{3} \delta_{ij} \frac{\partial u_k}{\partial x_k} \right].$$

Here, ρ is the mixture density, Y_m is the mass fraction of species m , $u_i = (u, v, w)$ is the mass-averaged mixture velocity, p is the pressure, D is the Fickian diffusivity, μ is the dynamic viscosity and $g_i = (0, 0, -g)$ is the acceleration.

2.2. Large-eddy equations

In DNS, (2.1) and (2.2) are solved with μ and D sufficiently large (or the domain sufficiently small) to resolve all flow gradients on the computational grid. In LES, the small scales of motion are (conceptually) removed from the problem by applying a low-pass filter to the governing equations. The resulting large-eddy equations are then solved for the large-scale features of the flow. The effects of subgrid-scale (SGS) motions on the resolved scales are modelled. A homogeneous LES filter is defined by the convolution

$$\bar{f}(\mathbf{x}) \equiv \int_{\mathcal{D}} G(|\mathbf{x} - \boldsymbol{\xi}|; \bar{\Delta}) f(\boldsymbol{\xi}) d\boldsymbol{\xi}, \quad (2.3)$$

where \mathcal{D} is the flow domain. The filter kernel is normalized,

$$\int_{-\infty}^{\infty} G(\xi; \bar{\Delta}) d\xi = 1,$$

and has a characteristic width, $\bar{\Delta}$, directly related to the LES grid spacing. For constant $\bar{\Delta}$ (uniform grid spacing), the filter commutes with derivatives and application of the filter to (2.1) and (2.2) results in

$$\frac{\partial \bar{\rho} \tilde{Y}_m}{\partial t} + \frac{\partial \bar{\rho} \tilde{Y}_m \tilde{u}_j}{\partial x_j} = \frac{\partial}{\partial x_j} \left(\bar{\rho} D \frac{\partial \tilde{Y}_m}{\partial x_j} + \eta_{mj} \right), \quad (2.4)$$

$$\frac{\partial \bar{\rho} \tilde{u}_i}{\partial t} + \frac{\partial \bar{\rho} \tilde{u}_i \tilde{u}_j}{\partial x_j} = -\frac{\partial \bar{p}}{\partial x_i} + \frac{\partial}{\partial x_j} (\bar{\tau}_{ij} + \sigma_{ij}) + \bar{\rho} g_i, \quad (2.5)$$

where

$$\eta_{mj} = \bar{\rho} (\tilde{Y}_m \tilde{u}_j - \widetilde{Y_m u_j}), \quad (2.6)$$

$$\sigma_{ij} = \bar{\rho} (\tilde{u}_i \tilde{u}_j - \widetilde{u_i u_j}), \quad (2.7)$$

with the tilde denoting a mass-weighted filter, e.g. $\tilde{u}_i = \overline{\rho u_i} / \bar{\rho}$. Additional elements arising from filtering the viscous and diffusive terms have been neglected. We model the SGS fluxes as

$$\eta_{mj} = \bar{\rho} D_T \frac{\partial \tilde{Y}_m}{\partial x_j}, \quad (2.8)$$

$$\sigma_{ij} = \mu_T \left[\frac{\partial \tilde{u}_i}{\partial x_j} + \frac{\partial \tilde{u}_j}{\partial x_i} - \frac{2}{3} \delta_{ij} \frac{\partial \tilde{u}_k}{\partial x_k} \right], \quad (2.9)$$

where D_T and μ_T are grid-dependent diffusivity and viscosity, respectively. Replacing \bar{u}_i with \tilde{u}_i in the expression for $\bar{\tau}_{ij}$, the large-eddy equations become

$$\frac{\partial \bar{\rho} \tilde{Y}_m}{\partial t} + \frac{\partial \bar{\rho} \tilde{Y}_m \tilde{u}_j}{\partial x_j} = \frac{\partial}{\partial x_j} \left[\bar{\rho} (D + D_T) \frac{\partial \tilde{Y}_m}{\partial x_j} \right], \quad (2.10)$$

$$\frac{\partial \bar{\rho} \tilde{u}_i}{\partial t} + \frac{\partial \bar{\rho} \tilde{u}_i \tilde{u}_j}{\partial x_j} = - \frac{\partial \bar{p}}{\partial x_i} + \frac{\partial}{\partial x_j} \left[(\mu + \mu_T) \left(\frac{\partial \tilde{u}_i}{\partial x_j} + \frac{\partial \tilde{u}_j}{\partial x_i} - \frac{2}{3} \delta_{ij} \frac{\partial \tilde{u}_k}{\partial x_k} \right) \right] + \bar{\rho} g_i. \quad (2.11)$$

These LES equations are identical to the DNS equations, except for the grid-dependent viscosity and diffusivity. Models for D_T and μ_T are discussed in § 2.3. The equations are solved using a tenth-order compact (Padé) scheme for the spatial derivatives and a third-order pressure-projection scheme for time advancement. An explicit filter is applied to ρ and ρu_i after each complete time step to reduce aliasing errors. Details of the numerical algorithm and filtering are given in the Appendices.

2.3. Subgrid-scale modelling

For ease of notation, the bars and tildes, denoting LES variables, will be dropped for the remainder of the paper. In constructing expressions for μ_T and D_T , we do not presume to represent the true physics of subgrid-scale motions. The goal here is simply to damp Gibbs oscillations (a result of the near sharp wavenumber cutoff of the LES filter) without corrupting the spectral energy flux at low and moderate wavenumbers. The efficacy of this LES approach relies on the premise that energy production at low and moderate wavenumbers, in conjunction with adequate representation of inertial-range dynamics, is sufficient to yield the correct growth rate and net mixing rate for this flow. For positive D_T and μ_T , (2.8) and (2.9) are purely dissipative. The optimal LES result with such modelling is a flow in which the inertial range of the energy spectrum extends up to the Nyquist wavenumber of the grid. In practice, a numerical dissipation range must be admitted at high wavenumbers, in order to remove energy that would otherwise pile up near the grid scale. The dissipation range can be made narrow (hence allowing for a broader inertial range) by imparting a high-wavenumber bias to the artificial viscosity (a hyperviscosity). Such high-wavenumber damping has been successfully employed in acoustics computations by Barone & Lele (2002) who constructed a dissipation operator based on the sixth derivative of the velocity field and applied the operator along grid lines. Here, we take a similar but less direct approach, wherein μ_T (rather than σ_{ij}) is based on the large derivative. This is done in order to retain the Navier–Stokes form of the momentum equation.

The particular SGS viscosity employed in our simulations is

$$\mu_T = C_\mu \overline{\rho \Delta^{r+1} S}, \quad (2.12)$$

where

$$S \equiv (S_{ij} S_{ij})^{1/2}, \quad S_{ij} \equiv \frac{1}{2} \left(\frac{\partial^r u_i}{\partial x_j^r} + \frac{\partial^r u_j}{\partial x_i^r} \right),$$

and the double overbar denotes a Gaussian filter (see Appendix B) that smooths out oscillations in μ_T . The length scale, $\Delta = \sqrt{\Delta x^2 + \Delta y^2 + \Delta z^2}$, is the effective grid spacing. The r parameter is set to 8, which provides a k^8 weighting of the viscosity in Fourier space (Cook & Cabot 2004). The eighth derivative is computed with the following compact scheme

$$\begin{aligned} 29\bar{u}_j^{VIII} + 14(\bar{u}_{j+1}^{VIII} + \bar{u}_{j-1}^{VIII}) + (3/2)(\bar{u}_{j+2}^{VIII} + \bar{u}_{j-2}^{VIII}) \\ = [4200\bar{u}_j - 3360(\bar{u}_{j+1} + \bar{u}_{j-1}) + 1680(\bar{u}_{j+2} + \bar{u}_{j-2}) \\ - 480(\bar{u}_{j+3} + \bar{u}_{j-3}) + 60(\bar{u}_{j+4} + \bar{u}_{j-4})]/\Delta_i^8, \end{aligned}$$

where Δ_i is the grid spacing in the i -direction and \bar{u}_j^{VIII} approximates the eighth derivative at the j th grid point (in the i -direction). The constant of proportionality is set to $C_\mu = 0.01$, a value judged optimal from a variety of tests on many flows including the Taylor–Green vortex. The large (eighth) derivative serves as a ringing detector; i.e. μ_T is only active where velocity gradients must be limited to remain resolved on the grid.

The SGS diffusivity, D_T , is designed to reduce the overshoots and undershoots in the filtered mass fractions. It was originally modelled in a similar fashion to μ_T (based on $\partial^8 Y_m / \partial x_j^8$); however, it was discovered that a cheaper and more effective method is to use the overshoots and undershoots directly. Hence, the SGS diffusivity employed in our simulations is

$$D_T = C_D \frac{\Delta^2}{\Delta t_{CFL}} \overline{\overline{\eta}}, \quad (2.13)$$

where

$$\eta = \begin{cases} -Y_2 & \text{if } Y_2 < 0, \\ 0 & \text{if } 0 \leq Y_2 \leq 1, \\ Y_2 - 1 & \text{if } Y_2 > 1, \end{cases}$$

the time scale, Δt_{CFL} , is the CFL condition

$$\Delta t_{CFL} = \min \left[\left(\frac{|u|}{\Delta x} + \frac{|v|}{\Delta y} + \frac{|w|}{\Delta z} \right)^{-1} \right], \quad (2.14)$$

and the triple overbar denotes a smoothing filter that fills in gaps between the over and undershoots (see Appendix B). By employing Δt_{CFL} as the diffusion time scale, the oscillations can be damped in the most rapid manner possible without violating stability limits on diffusion. The diffusion constant is set to $C_D = 1000$, which strongly inhibits the mass fractions from straying out of bounds. With this prescription for D_T , the overshoots and undershoots, normally about 10% for Gibbs oscillations, are reduced to less than 1%.

3. Definitions

3.1. Dominant wavelength

With homogeneity (periodic boundaries) in x and y , ensemble averages (denoted by angle brackets) are equivalent to horizontal integrals, i.e. for any variable $\phi(x, y, z, t)$ in an L^3 box,

$$\langle \phi \rangle(z, t) = \frac{1}{L^2} \int_0^L \int_0^L \phi(x, y, z, t) dx dy. \quad (3.1)$$

The number of independent realizations in the ensemble is determined by the width of the autocorrelation function for ϕ . The correlation width is closely related to the dominant wavelength

$$\lambda_\phi(t) \equiv \frac{\int_0^{k_{max}} E_\phi(k, 0, t)/k \, dk}{\int_0^{k_{max}} E_\phi(k, 0, t) \, dk}, \quad (3.2)$$

where $k = \sqrt{k_x^2 + k_y^2}$ is the magnitude of horizontal wavevectors associated with an annulus in Fourier space and E_ϕ is the two-dimensional energy spectrum of $\phi' = \phi - \langle \phi \rangle$, computed by taking the Fourier transform of ϕ' , multiplying by its complex conjugate, and summing over the annulus associated with each wavenumber bin. The box width, L , is normalized to 2π , such that $k=1$ corresponds to the fundamental mode. In an LES, k_{max} is taken as the Nyquist wavenumber; however, in an experiment or DNS, k_{max} should be set to the wavenumber at which diffusion or surface tension reduces the growth rate to zero, according to linear stability theory. If $\lambda_\phi \ll L$, then accurate averages can be computed for ϕ and the periodic boundaries will not restrict the growth of λ_ϕ .

3.2. Mixing height

The amount of mixed fluid is quantified by considering a passive, equilibrium chemical reaction between the light and heavy fluids. An example of such a reaction is the $\text{HCl} + \text{NaOH} \rightarrow \text{H}_2\text{O} + \text{NaCl}$ reaction for the pH indicator in the experiments of Linden, Redondo & Youngs (1994). The mole fraction of heavy fluid is

$$X = \frac{\rho - \rho_1}{\rho_2 - \rho_1}, \quad (3.3)$$

and the mole fraction of product is

$$X_p(X) = \begin{cases} X/X_{st} & \text{if } X \leq X_{st}, \\ (1-X)/(1-X_{st}) & \text{if } X > X_{st}, \end{cases} \quad (3.4)$$

where X_{st} is the heavy-fluid mole fraction for a stoichiometric mixture, which is set to the equimolar value $X_{st} = 1/2$. The height of the mixing region is defined as the product thickness that would result if the entrained fluids were perfectly mixed in x and y , i.e.

$$h \equiv \int_{-\infty}^{\infty} X_p(\langle X \rangle) \, dz. \quad (3.5)$$

Thus, h is an entrainment length, derived from the volumes of pure fluids entering the mixing region. Now let ζ be the z location where $\langle X \rangle = X_{st}$ and let the interface be initially located at $z=0$. The mixing height can be divided into two lengths, $h = h_b - h_s$, corresponding to the volumes of light and heavy fluid crossing the $z=0$ plane, i.e.

$$-h_s = \int_{-\infty}^{\min(0, \zeta)} \langle X \rangle / X_{st} \, dz + \int_{\min(0, \zeta)}^0 (1 - \langle X \rangle) / (1 - X_{st}) \, dz, \quad (3.6)$$

$$h_b = \int_0^{\max(0, \zeta)} \langle X \rangle / X_{st} \, dz + \int_{\max(0, \zeta)}^{\infty} (1 - \langle X \rangle) / (1 - X_{st}) \, dz. \quad (3.7)$$

In subsequent sections, we will demonstrate the relationship between these integral definitions and the more common ‘spike’ and ‘bubble’ threshold definitions,

$$\langle X \rangle(z = -h_s^{n\%}) = n\%, \quad (3.8)$$

$$\langle X \rangle(z = h_b^{n\%}) = 1 - n\%. \quad (3.9)$$

3.3. Progress variable

It is instructive to measure growth of the mixing region in units of the dominant perturbation wavelength. The simulated flow is initially quiescent, perturbed only in the density field; hence, the dominant initial wavelength is $\lambda_o = \lambda_\rho(0)$. A natural progress variable is h/λ_o , with corresponding timescale

$$\tau \equiv \left(\frac{\lambda_o}{Ag} \right)^{1/2}, \quad (3.10)$$

where

$$A = \frac{\rho_2 - \rho_1}{\rho_2 + \rho_1} = \frac{1}{2} \quad (3.11)$$

is the Atwood number used in this study.

3.4. Mixing variables

The relative amount of molecularly mixed fluid within the mixing zone is typically characterized as the ratio of a mixing length to an entrainment length. Youngs (1994) defines the ratio to be

$$\Theta \equiv \frac{\int_{-\infty}^{\infty} \langle X(1-X) \rangle dz}{\int_{-\infty}^{\infty} \langle X \rangle \langle 1-X \rangle dz}, \quad (3.12)$$

whereas Cook & Dimotakis (2001) use

$$\Xi \equiv \frac{\int_{-\infty}^{\infty} \langle X_p \rangle dz}{h}. \quad (3.13)$$

We will show that Θ and Ξ give very similar measures of the state of mixing within the layer.

Another quantity related to mixing is the effective Atwood number, which we define at the mid-plane by

$$A_e \equiv \frac{\rho_{rms}}{\langle \rho \rangle|_0}, \quad (3.14)$$

where $\langle \rho \rangle|_0 = \langle \rho \rangle(z = 0)$ and

$$\rho_{rms} = \langle \rho'^2 \rangle^{1/2}|_0, \quad \rho' = \rho - \langle \rho \rangle. \quad (3.15)$$

When A_e decreases, the two fluids are diffusing together faster than pure fluids are being brought to the mid-plane. Conversely, when A_e increases, pure fluids are coming into contact with the mid-plane faster than they are mixing by diffusion. For immiscible fluids, $A_e \approx A$ assuming $\langle \rho \rangle|_0 \approx (\rho_1 + \rho_2)/2$.

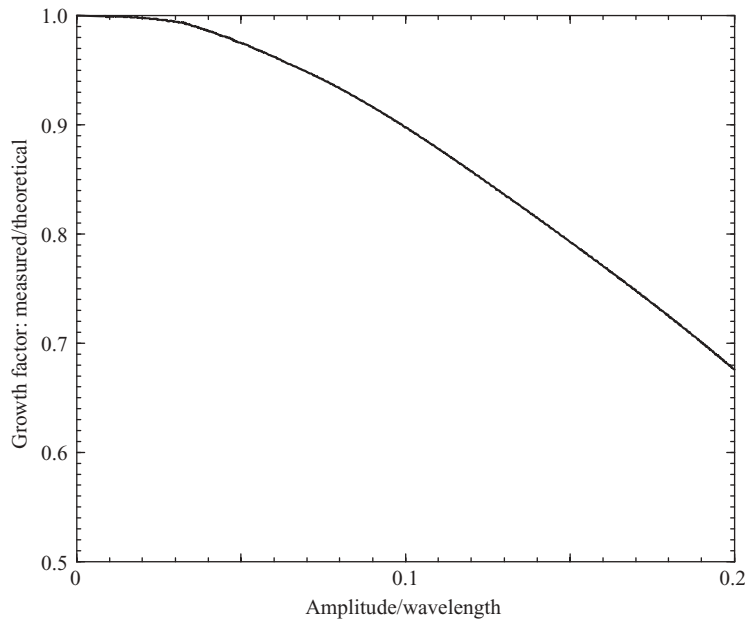


FIGURE 1. Growth factor, \dot{h}_a/h_a , where the amplitude h_a is half the peak-to-valley height of the mean density level, $(\rho_1 + \rho_2)/2$, normalized by the growth factor from linear stability theory, $\sqrt{Agk/\psi}$, with $A = 1/2$, $g = 1$, $k = 1$ (fundamental mode) and $\psi = 1.03$ (thickness correction) (Duff *et al.* 1962).

4. Verification and validation

4.1. Comparison with linear stability theory

We have verified that the LES methodology produces growth rates in agreement with linear stability theory for single-mode Rayleigh–Taylor instability. The growth rate factor from a 512^2 point single-mode simulation was compared to the theoretical growth rate factor from Duff *et al.* (1962) for an interface with small initial thickness. In the simulation, μ and D were set to zero, but μ_T , D_T and the filter were all active. In figure 1, the measured/theoretical growth factor is plotted versus amplitude/wavelength. For amplitude to wavelength ratios of less than 3 %, simulation and theory agree to within 1 %. At larger ratios, nonlinear effects become important and agreement drops off.

4.2. Comparison with DNS

In addition to comparing with linear stability theory, we confirmed that the LES converges to DNS at low Schmidt and Reynolds numbers. In testing this convergence, a 256^3 DNS was conducted of Rayleigh–Taylor instability for a case very similar to that described in Cook & Zhou (2002), i.e. $A = 1/2$ with isotropic perturbations peaked at mode 16. An accompanying LES was performed with a set-up identical to the DNS, but with the filter and SGS models active. The DNS ran stably until a time of $t = 7.33\tau$ before crashing owing to inadequate small-scale resolution. Volume renderings of the lower fluid at $t = 7.25\tau$ are displayed in figure 2 for both simulations. The flows appear identical, based on visual inspection, suggesting that convergence is achieved. The bubble and spike heights for the DNS and LES are plotted in figure 3. The filter and SGS models preserve the DNS growth rates while enabling the LES to proceed to Reynolds numbers well beyond the reach of DNS.

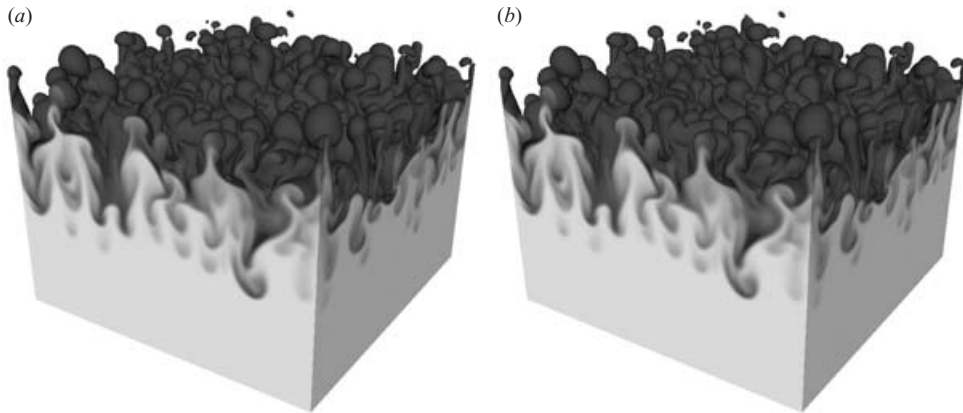


FIGURE 2. Volumes of $\rho \leq 2.5$ fluid from (a) DNS and (b) LES.

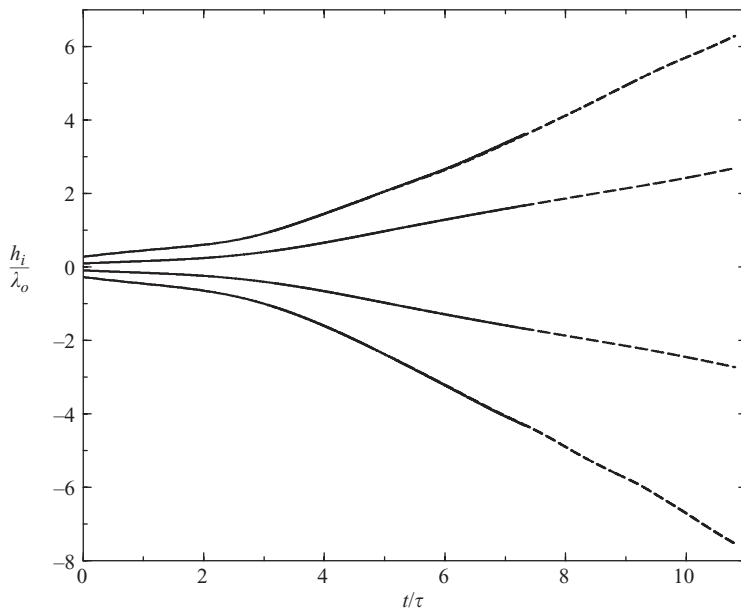


FIGURE 3. Mixing heights from validation DNS (solid) and LES (dashed). Top and bottom curves are $h_b^{1\%}$ and $-h_s^{1\%}$, respectively. Middle curves are h_b and $-h_s$.

4.3. Wall effects

The influence of the top and bottom walls on the growth of the mixing layer was assessed by performing two identical simulations, with the domain height doubled in the second set-up. Figure 4 displays the heights of the bubbles and spikes in each case. The results of this test suggest that the walls do not affect the growth of the mixing region until the tips of the bubbles and spikes approach the ends of the domain.

5. Simulation details

The computational domain for the production LES is an L^3 cube composed of 1152^3 uniformly spaced grid points. Acceleration is set to $g=1$ and the densities

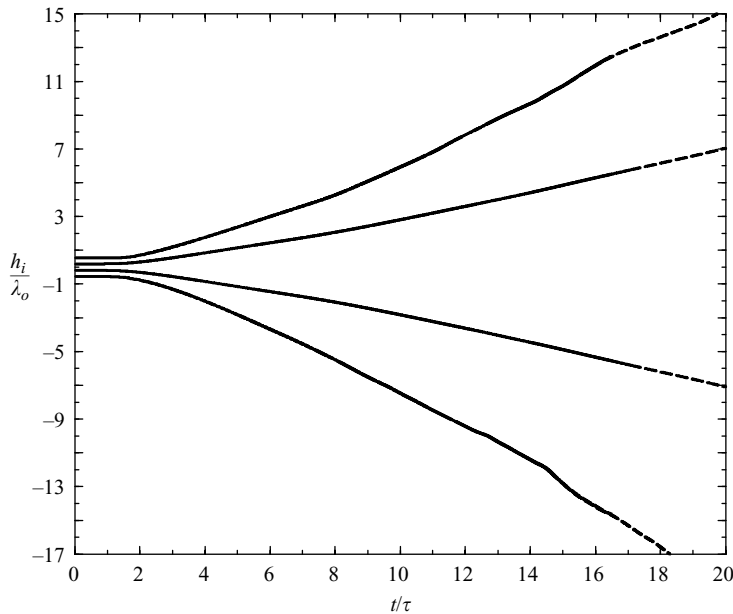


FIGURE 4. Mixing heights for simulations with 256^3 (solid) and $256^2 \times 512$ (dashed) grid points. The top and bottom of the bounding box correspond to the locations of the walls in the 256^3 simulation. Top and bottom curves are $h_b^{1\%}$ and $-h_s^{1\%}$, respectively. Middle curves are h_b and $-h_s$.

of the light and heavy fluids are set to $\rho_1 = 1$ and $\rho_2 = 3$, respectively. Boundary conditions are periodic in x and y , with no-slip walls imposed in z at the top and bottom of the box. The initial fluid interface is prescribed as an error function,

$$\rho(\mathbf{x}, 0) = \frac{1}{2}[\rho_1 + \rho_2 + (\rho_2 - \rho_1)\text{erf}(z/\epsilon + \xi(x, y))], \quad \epsilon = 5\Delta z/2, \quad (5.1)$$

where Δz is the grid spacing in z and $\xi(x, y)$ is a field of isotropic perturbations, which are fit to the Gaussian spectrum shown in figure 5. The root-mean-square of the perturbations is

$$\left[2 \int_0^{k_{max}} E_\xi(k) dk\right]^{1/2} = 0.1.$$

Setting $L = 2\pi$, then $k_{max} = 576$ corresponds to the Nyquist wavenumber. The perturbation spectrum peaks at $k = 144$ with standard deviation $\sigma_k = 24$. The initial perturbations on the $z = 0$ plane are shown in figure 6. To allow the fine-scale perturbations to grow, free from viscous and diffusive damping, μ and D are both set to zero. This initialization is chosen to place the flow as far as possible into the ‘mode-coupling’ limit, while still providing adequate resolution of the initial perturbations.

The simulation proceeds until the dominant (most energetic) flow structures approach L . We report results up to $t/\tau = 33$ ($h/\lambda_0 \approx 30$), where we have confidence that the results are independent of both vertical and horizontal flow boundaries. At this time, the horizontal autocorrelation of vertical velocity at half-domain separation is still below 10%, and there are about five large-scale structures in the box.

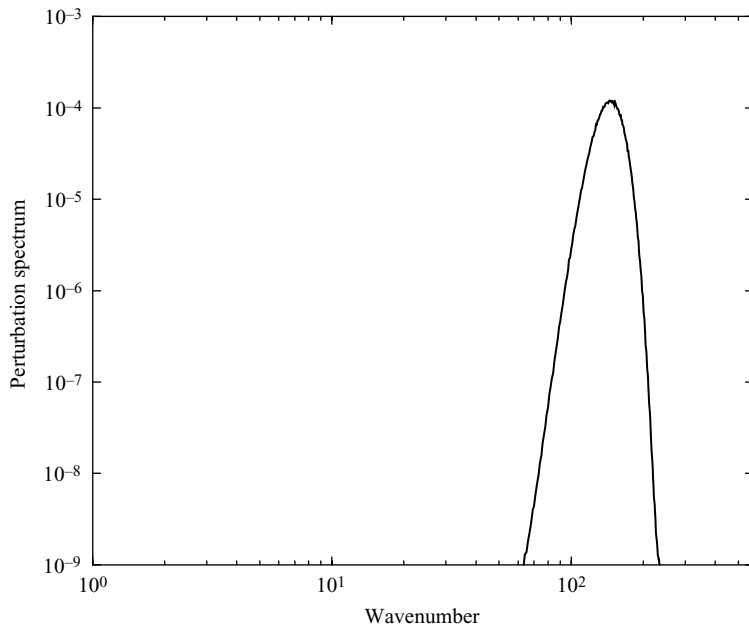


FIGURE 5. Spectrum of initial interfacial perturbations.

6. Results

6.1. LES variables

The density and vorticity fields develop large dynamical ranges, as indicated in figure 7, which also shows the roles μ_T and D_T play in the LES. The SGS diffusivity is most active at the bubble and spike fronts since that is where density gradients are largest. The SGS viscosity, on the other hand, is most active inside the layer since that is where velocity gradients are steepest.

6.2. Growth stages

The evolution of the instability is depicted in figure 8, which shows side-on views of the mixing layer at four different times during the course of the simulation. At early times, the perturbations grow in a fairly independent fashion (figure 8a). Then the modes begin to couple to one another and secondary Kelvin–Helmholtz instabilities appear (figure 8b). At this point, the range of scales in the mixing layer rapidly increases, generating more mixed fluid within the layer (figure 8c). We regard this phenomenon as qualitative evidence of the mixing transition (Dimotakis 2000). Post transition, the large scales in the flow (bubble/spike diameters) continue to increase until the mixing region becomes fully turbulent (figure 8d).

The effect of mixing on the RTI growth rate is illustrated in figure 9, where A_e is seen to correlate with the bubble/spike growth rate. The curves for \dot{h}_s and \dot{h}_b are computed by taking time derivatives of (3.6) and (3.7). The near equivalence of \dot{h}_s and \dot{h}_b demonstrates how the integral definition reduces the asymmetry compared to the 1 % threshold definition. Four stages of growth, corresponding to the images shown in figure 8, are labelled in the figure. We identify these stages as: (I) independent modal growth, (II) weak turbulence, (III) mixing transition, and (IV) strong turbulence. In stage I, the perturbations increase in magnitude, but remain essentially independent from one another. In stage II the modes begin to couple as secondary

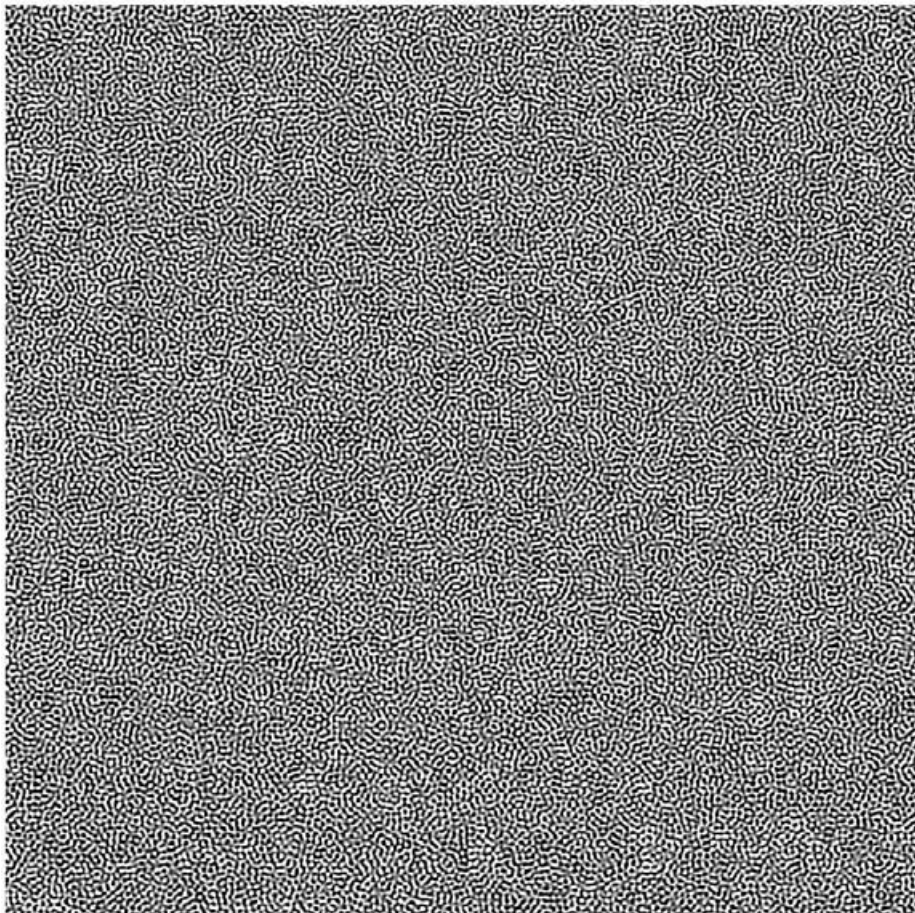


FIGURE 6. Initial perturbations on $z = 0$ plane.

Kelvin–Helmholtz instabilities develop. In stage III, the mixing rate overtakes the entrainment rate (downward slope of A_e/A), which temporarily reduces the growth rate. Finally, in stage IV, mixing and entrainment rates come into balance and the layer experiences a boost in growth.

6.3. Layer height

Figure 10 displays the spike and bubble heights as a function of t/τ . It is demonstrated that $h_s^{1\%}$ and $h_b^{1\%}$ can both be obtained by multiplying the integral height, h , by constant factors; these factors, however, probably vary with Atwood number. The total mixing height, h , and the dominant horizontal density wavelength, λ , are plotted in figure 11. The dominant horizontal scales are seen to grow at approximately the same rate as the mixing height. Lines are drawn at the boundaries of the stages defined in figure 9 to assist in mapping the time variable, t/τ , onto the progress variable, h/λ_o .

6.4. Mixing transition

Figure 12 displays the mixing variables (3.12, 3.13) as functions of the progress variable, h/λ_o . Both Θ and Ξ provide essentially the same measure of the amount of

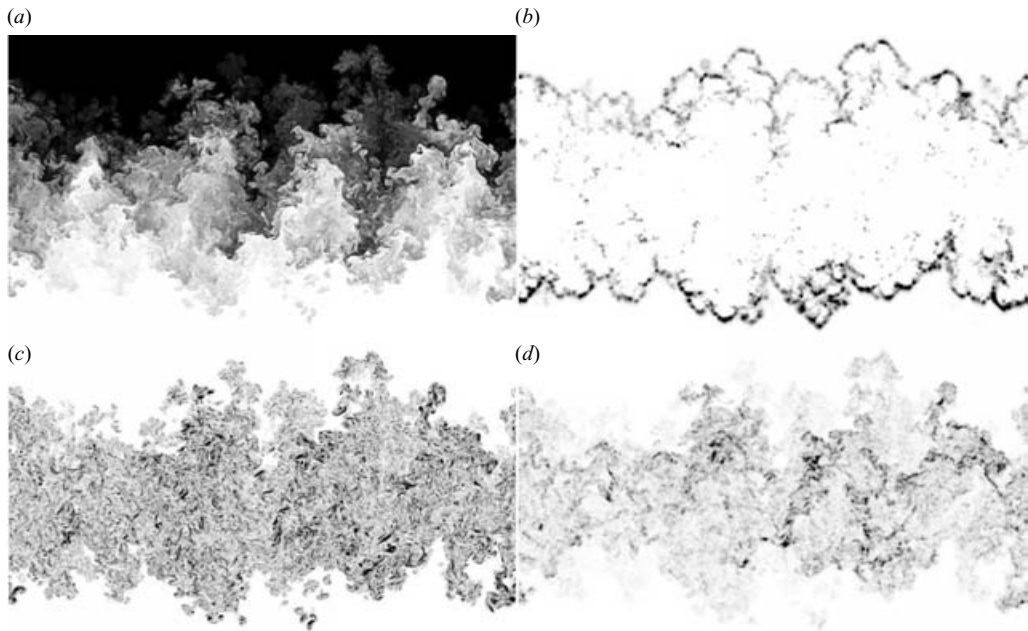


FIGURE 7. Side-on views of mixing region at $t/\tau = 33$. (a) Density (ρ) (b) SGS diffusivity (D_T), (c) vorticity magnitude ($\|\nabla \times \mathbf{u}\|$), and (d) SGS viscosity (μ_T).

molecularly mixed fluid within the layer. The mixing transition corresponds to the rise in Θ and Ξ for the range $6 < h/\lambda_o < 15$. Further quantitative evidence for the mixing transition is observed in the evolution of the probability density function (p.d.f.) of the heavy-fluid mole fraction. Figure 13 displays the p.d.f. of X at two instances before and two instances after the transition. A significant increase in mixed fluid occurs during stage III, after which there is little change in the p.d.f. Similar behaviour has been observed in turbulent jets for Reynolds numbers spanning 3000 to 24 000 (Miller & Dimotakis 1991), and in other flows described by Dimotakis (2000). The increase in mixed fluid during stage III corresponds to formation of an inertial range in the two-dimensional spectrum of the vertical velocity component, w . The w spectrum on the $z=0$ plane is plotted in figure 14 at times corresponding to the ends of the first three growth phases. In stage I, the perturbation spectrum increases in magnitude, but the peak remains close to λ_o . In stage II the peak of the spectrum begins migrating to lower wavenumbers, and in stage III an inertial range forms. Dimotakis (2000) has noted that formation of an inertial range tends to occur simultaneously with an increase in mixed fluid for a wide variety of flows. We observe similar behaviour for Rayleigh–Taylor instability.

6.5. Spectra

In figure 15, late-time velocity and density spectra are plotted. The ρ and w spectra develop fairly broad power-law ranges during stage IV. The difference in magnitude between E_ρ and E_w is a consequence of the boundedness of ρ ; i.e. $\rho_1 \leq \rho \leq \rho_2$, whereas w is unbounded (Dimotakis & Miller 1990). The energy spectra of u and v appear to lag the w spectrum in development, falling below the w spectrum at low wavenumbers

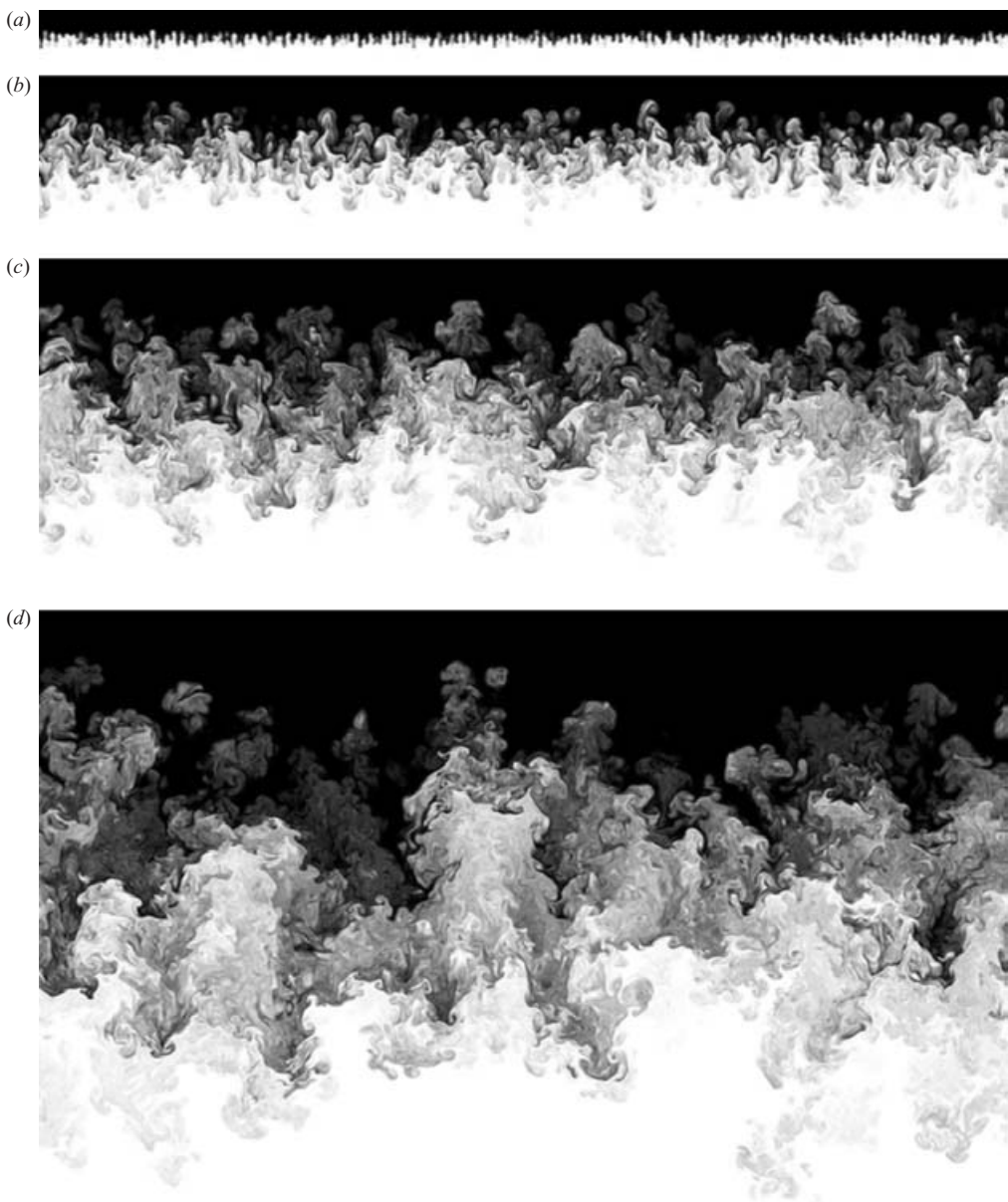


FIGURE 8. Side-on views of density in the mixing region for stages I–IV (*a–d*). Times displayed are $t/\tau = 3, 11, 21$ and 33 . Heavy fluid is black.

but approaching the w spectrum at high wavenumbers. The secondary flow develops more quickly at high wavenumbers as a result of more rapid eddy turnovers. As time advances, the u and v spectra conform to the w spectrum at progressively larger scales. This same wavenumber-dependent lag between the horizontal and vertical velocity spectra has been observed experimentally by Ramaprabhu & Andrews (2004).

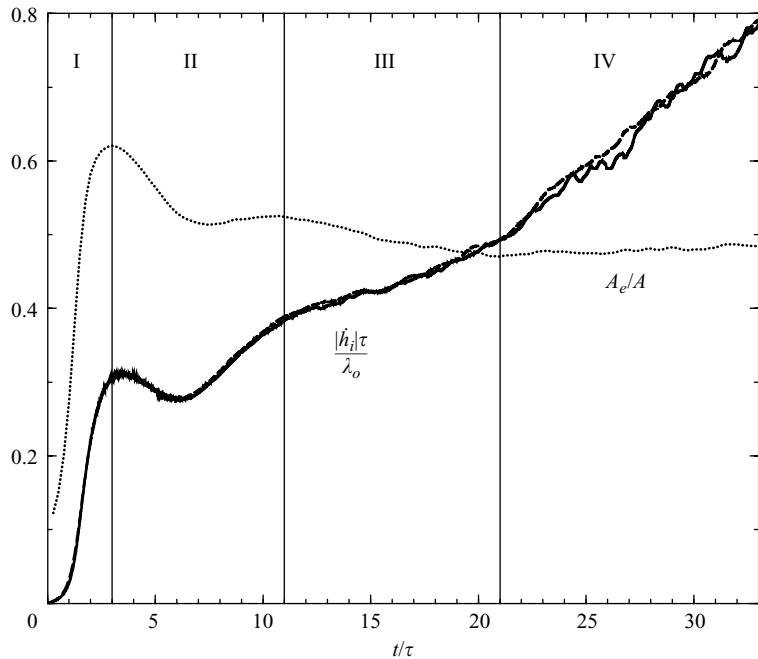


FIGURE 9. Growth rate of bubbles (\dot{h}_b , solid line) and spikes (\dot{h}_s , dashed line), along with effective Atwood number ratio (A_e/A , dotted line).

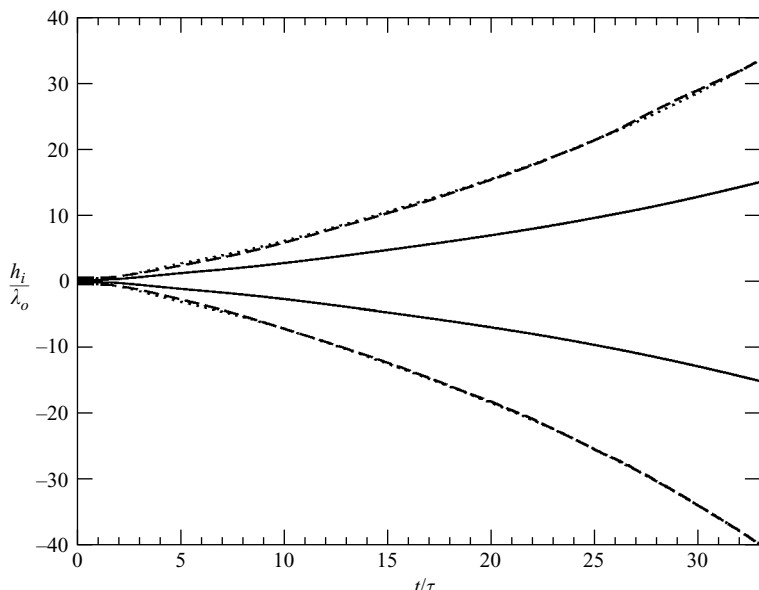


FIGURE 10. Bubble (upper) and spike (lower) heights vs. t/τ . Solid lines are h_b and $-h_s$. Dashed lines are $h_b^{1\%}$ and $-h_s^{1\%}$. Dotted lines (nearly coincident with dashed lines) are $1.112h$ and $-1.324h$, where h is defined in (3.5).

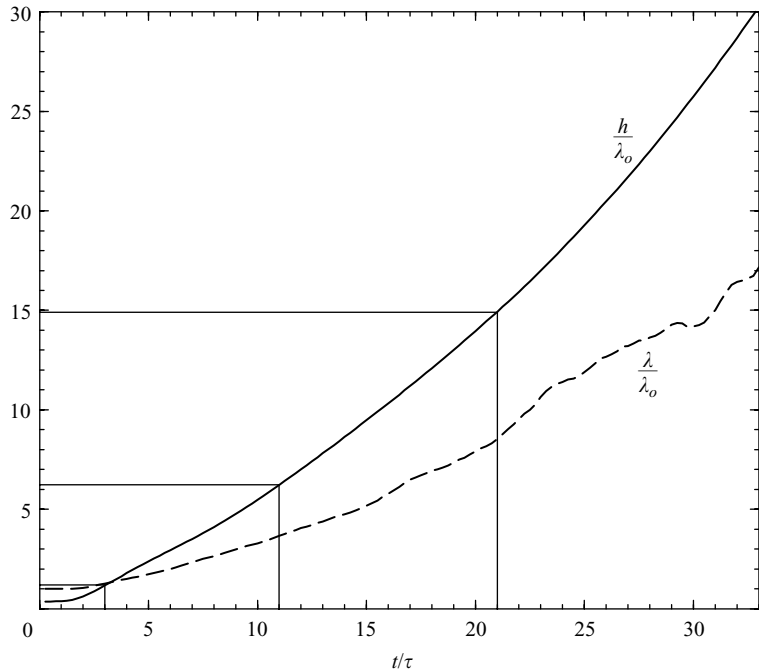


FIGURE 11. Time-evolution of mixing height, h , and dominant horizontal wavelength, λ . Fiducial lines delineate approximate growth-stage boundaries.

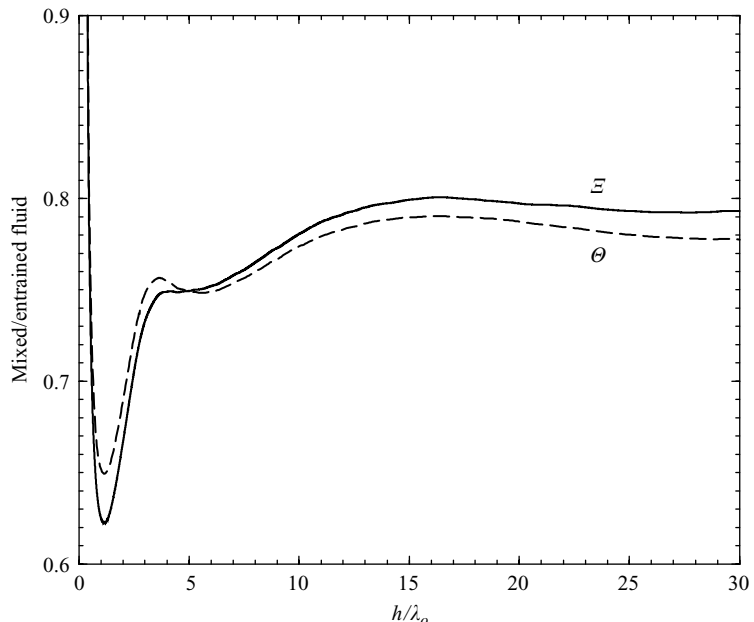


FIGURE 12. Ratio of mixed to entrained fluid for the mixing region. Θ , $\Xi = 1$ corresponds to completely mixed fluid (no horizontal variation), whereas Θ , $\Xi = 0$ corresponds to complete segregation (immiscible case).

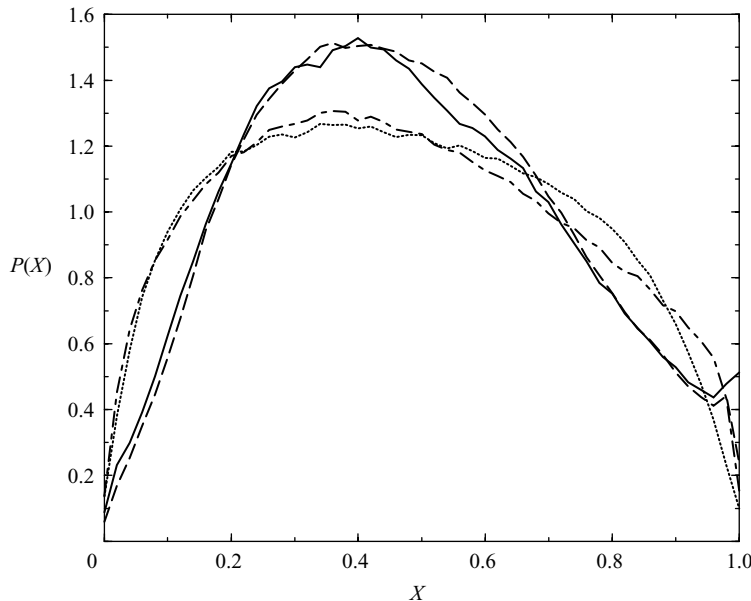


FIGURE 13. Probability density functions of heavy-fluid mole fraction on $z=0$ plane ($\dots, t = 7\tau; \cdots, t = 11\tau; ---, t = 21\tau; —, t = 33\tau$).

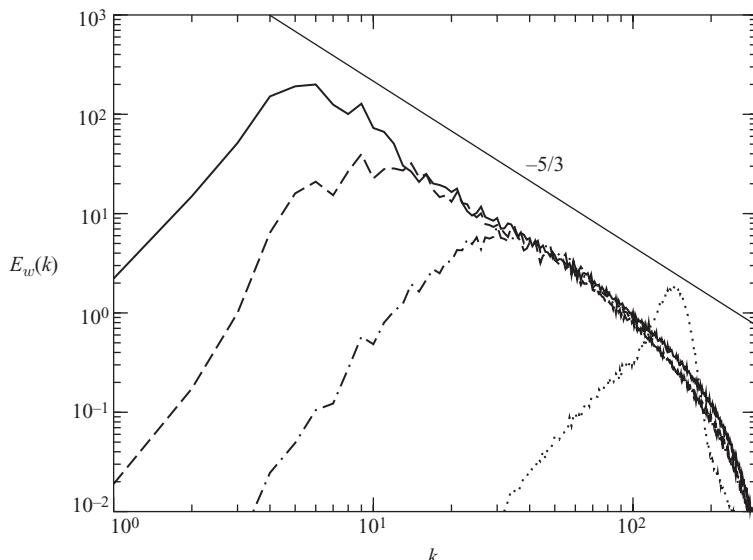


FIGURE 14. Evolution of the vertical velocity spectrum computed in the $z=0$ plane (key as for figure 13). A fiducial corresponding to $k^{-5/3}$ is drawn for reference.

6.6. Energy budget

The potential energy released into the flow is

$$PE(t) = \int_{L^3} [\rho(\mathbf{x}, 0) - \rho(\mathbf{x}, t)] g z d^3 \mathbf{x}, \quad (6.1)$$

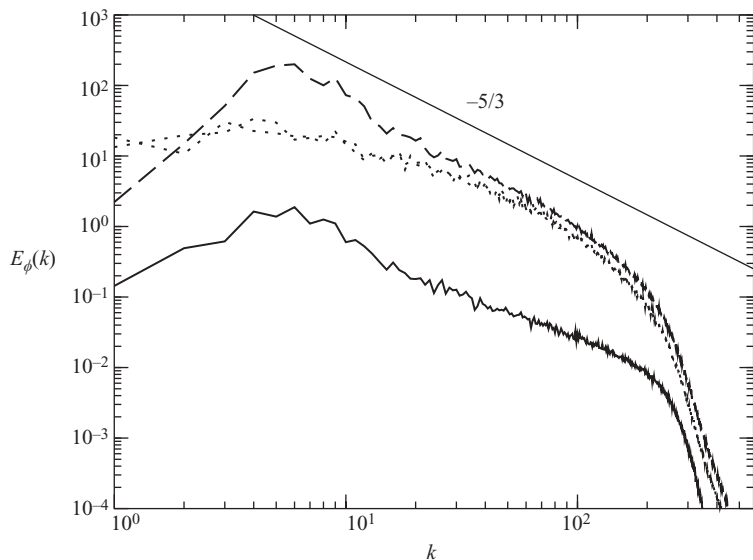


FIGURE 15. Two-dimensional spectra of density and velocity components in the $z=0$ plane at $t=33\tau$ ($h=30\lambda_o$). The solid line is ρ , the dashed line is w and the dotted lines are u and v . A fiducial corresponding to $k^{-5/3}$ is drawn for reference.

and the kinetic energy present in the flow is $KE = KE_{xy} + KE_z$, where

$$KE_{xy}(t) = \frac{1}{2} \int_{L^3} \rho [u^2 + v^2] d^3x \quad (6.2)$$

and

$$KE_z(t) = \frac{1}{2} \int_{L^3} \rho w^2 d^3x. \quad (6.3)$$

Ratios of kinetic energy to potential energy and horizontal energy to vertical energy are plotted in figure 16 versus the progress variable h/λ_o . The KE/PE ratio has not quite come into balance by $t/\tau = 33$; however, it has reached a value of 0.50 with a fairly shallow rise. This value is in close agreement with the experimental value of 0.51 measured by Ramaprabhu & Andrews (2004). The continued rise at late times is probably related to lack of an established inertial range in the secondary flow (u and v). The ratio of horizontal to vertical kinetic energy appears to reach an asymptotic value of 0.58 (also in agreement with experiment) by $h/\lambda_o = 21$.

6.7. Mole-fraction profiles

Figure 17 displays mole-fraction profiles at three different times during the course of the simulation. The profiles collapse to a universal function of z/h , indicating a degree of self-similarity in the layer development. Deviations from this universal curve are slight, suggesting that statistics are adequately converged. The mole-fraction profile reaches this self-similar state at very early time and does not appear significantly affected by the four stages of growth discussed previously. The slight asymmetry in the profiles is a consequence of the moderate Atwood number.

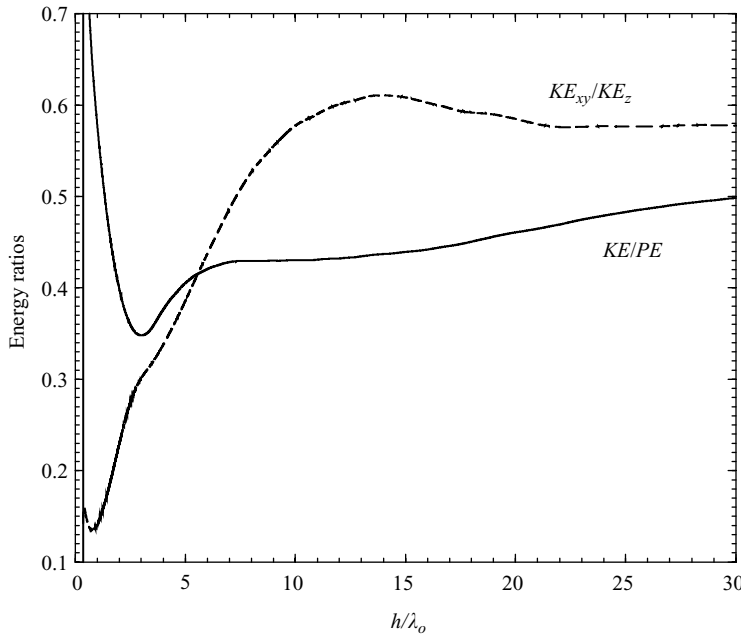


FIGURE 16. Ratios of total kinetic energy to released potential energy, and horizontal kinetic energy to vertical kinetic energy.

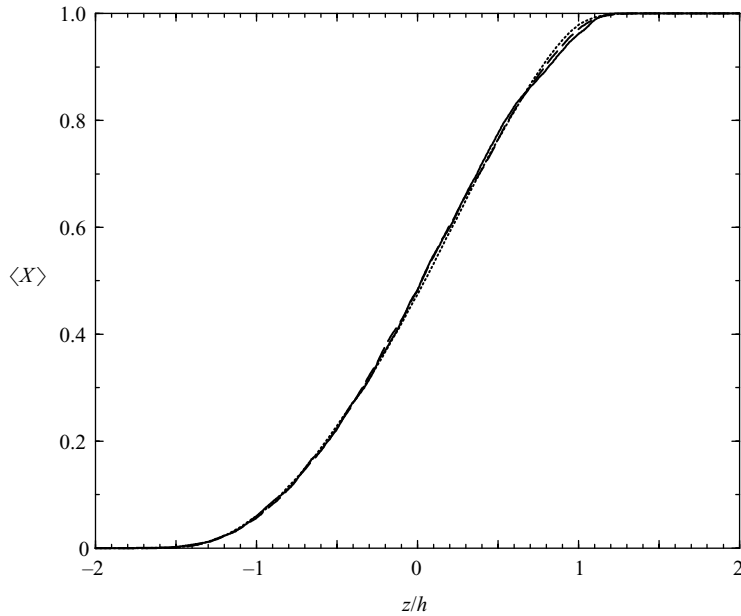


FIGURE 17. Heavy-fluid mole fraction averaged over horizontal planes (\dots , $t = 11\tau$; $--$, $t = 21\tau$; $-$, $t = 33\tau$).

7. Growth-mixing relation

7.1. Growth and mass flux

An approximate relationship between the degree of internal mixing and the growth rate of the turbulent region can be derived using mass continuity along with the

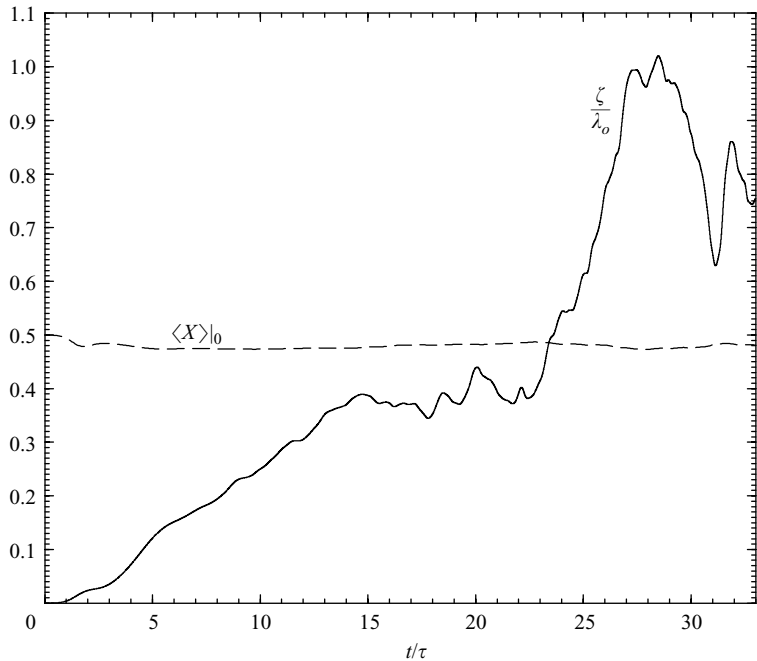


FIGURE 18. Mean mole fraction at $z=0$ (dashed line) and displacement of equimolar plane (solid line) versus t/τ .

definition of the integral mixing height. Differentiating (3.5) with respect to time results in

$$\dot{h} = \frac{1}{X_{st}} \int_{-\infty}^{\zeta} \frac{\partial \langle X \rangle}{\partial t} dz - \frac{1}{1-X_{st}} \int_{\zeta}^{\infty} \frac{\partial \langle X \rangle}{\partial t} dz, \quad (7.1)$$

Using the mean continuity equation,

$$\frac{\partial \langle \rho \rangle}{\partial t} + \frac{\partial \langle \rho w \rangle}{\partial z} = 0, \quad (7.2)$$

and $\langle \rho \rangle = \rho_1 + (\rho_2 - \rho_1)\langle X \rangle$ in (7.1) leads to the exact relation

$$\dot{h} = \frac{-1}{X_{st}(1-X_{st})(\rho_2 - \rho_1)} \frac{\langle \rho w \rangle|_{\zeta}}{\langle X \rangle|_{\zeta}}. \quad (7.3)$$

The net mass flux through the ($z=\zeta$)-plane, $\langle \rho w \rangle|_{\zeta}$, can be approximated by the net mass flux through the ($z=0$)-plane, $\langle \rho w \rangle|_0$, provided ζ is sufficiently close to 0 and/or the variation in $\langle \rho w \rangle$ is sufficiently small between these planes. Indeed, figure 18 shows that ζ/λ_o is typically less than unity, and figure 19 indicates that the mass flux varies little over the relevant range in z . Making this approximation, and using $X_{st} = 1/2$, results in

$$\dot{h} \approx \frac{-4 \langle \rho w \rangle|_0}{(\rho_2 - \rho_1)}. \quad (7.4)$$

Hence, the growth rate of the mixing layer can be viewed as the net mass flux through the ($z=0$)-plane. Neglecting diffusive effects, $\langle w \rangle = 0$; therefore, growth is associated with the correlation between density and vertical velocity at the mid-plane.

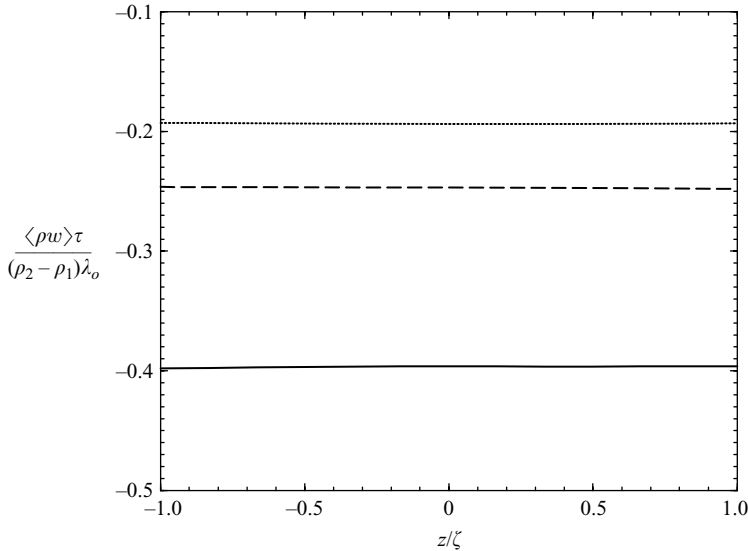


FIGURE 19. Net mass flux near the centre of the mixing region
 $(\dots, t = 11\tau; ---, t = 21\tau; —, t = 33\tau)$.

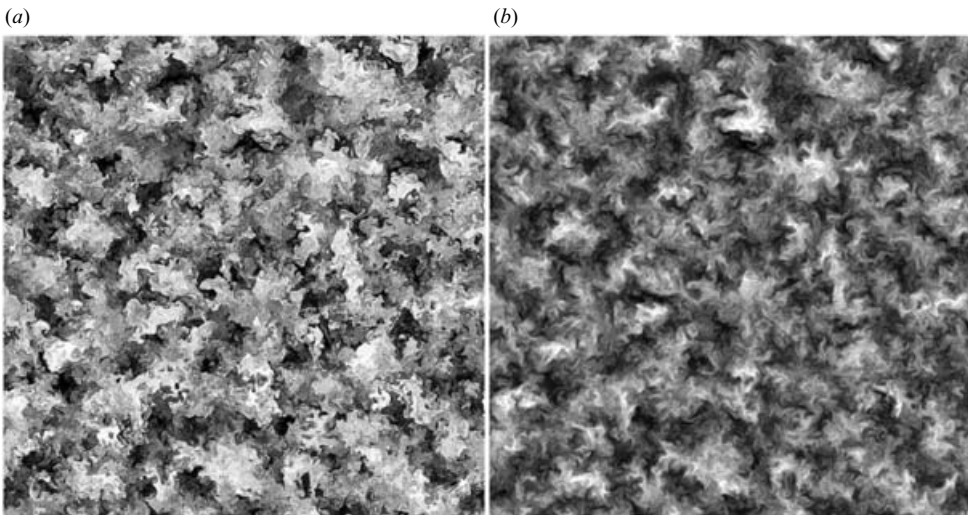


FIGURE 20. (a) Density and (b) downward velocity on the $(z = 0)$ -plane at $t = 26\tau$.

7.2. Mass flux and mixing

The governing equation for the mid-plane mass flux, $\langle \rho w \rangle|_0$, is given by the mean vertical momentum equation, but this introduces higher-order unknowns into the system, leading to the usual closure problem. Instead, we explore some empirical relations for the mid-plane mass flux in (7.4). We observe in figure 20 a strong correlation between density and negative vertical velocity at large scales. The correlation between ρ and $-w$,

$$C_r = \frac{-\langle \rho w \rangle|_0}{\rho_{rms} w_{rms}}, \quad (7.5)$$

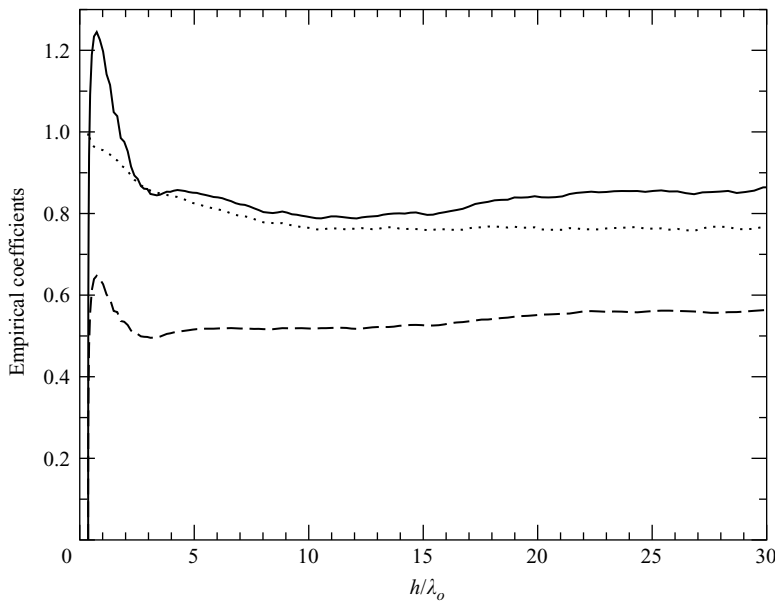


FIGURE 21. Dependence of empirical coefficients on flow development.
 ..., C_r (7.5); ---, C_w (7.8); —, $C = 2C_r C_w$.

is found in figure 21 to have a nearly constant value of 0.76 at late times ($h/\lambda_o > 21$). The r.m.s. density can be recast in terms of the effective Atwood number A_e , defined in (3.14), such that

$$\frac{\rho_{rms}}{\rho_2 - \rho_1} = \frac{\langle \rho \rangle|_0}{\rho_2 + \rho_1} \frac{A_e}{A}. \quad (7.6)$$

Figure 18 indicates that $\langle X \rangle|_0 \approx 1/2$, therefore

$$\frac{\langle \rho \rangle|_0}{\rho_2 + \rho_1} = (\langle X \rangle|_0 - \tfrac{1}{2}) A + \tfrac{1}{2} \approx \tfrac{1}{2}. \quad (7.7)$$

The validity of this approximation at larger Atwood numbers is yet to be determined. The ratio A_e/A reaches a nearly constant value of 0.48 at late times (see figure 9). A balance between kinetic and potential energy (in the spirit of buoyancy–drag models) suggests the following approximation for the mid-plane vertical velocity fluctuations,

$$w_{rms} = (\langle w^2 \rangle|_0)^{1/2} \approx C_w \sqrt{A_e g h}, \quad (7.8)$$

where C_w is an empirical constant with a value of about 0.56 at late times (see figure 21). Equation (7.8) is a generalization of the terminal velocity expression for a falling sphere with diameter $\propto \lambda \propto h$ (see figure 11). Experimental evidence demonstrating a link between w_{rms} and \dot{h} has been found by Ramaprabhu & Andrews (2004).

An approximate relation between growth and mixing is obtained by combining (7.4), (7.5), (7.7) and (7.8), yielding

$$\dot{h} \approx C \left(\frac{A_e}{A} \right)^{3/2} (A g h)^{1/2}, \quad (7.9)$$

where $C = 2C_r C_w \approx 0.85$. The solution to (7.9) is

$$h^{1/2} \approx h_c^{1/2} + \int_{t_c}^t \left(\frac{C}{2} \right) \left(\frac{A_e}{A} \right)^{3/2} (Ag)^{1/2} dt^*, \quad (7.10)$$

where $h_c = h(t_c)$. If C and A_e are assumed constant for $t \geq t_c$, then

$$h(t) \approx h_c + 2(\alpha Agh_c)^{1/2}(t - t_c) + (\alpha Ag)(t - t_c)^2, \quad (7.11)$$

where

$$\alpha = \left(\frac{C}{2} \right)^2 \left(\frac{A_e}{A} \right)^3. \quad (7.12)$$

The mixing layer thus exhibits both linear and quadratic growth rates, the prevalence of either depending on initial conditions. Glimm *et al.* (2001) arrive at an equation similar to (7.11) through a virtual shift in the starting time. Inserting $C = 0.85$ and $A_e = 0.48A$ into (7.12) yields $\alpha \approx 0.020$, or, in terms of the 1 % bubble height (see figure 10) $\alpha_b \approx 0.022$. A direct measure of α , from the slope of \dot{h} for $t/\tau > 21$ in figure 9, yields $\alpha = 0.025$, corresponding to $\alpha_b \approx 0.027$. These values are near the low end of the range of measurements reported in the literature, but are consistent with the general downward trend for simulations of increasing resolution (Dimonte *et al.* 2004).

7.3. Immiscible case

For immiscible fluids, ρ_{rms} attains its maximum possible value,

$$\max(\rho_{rms}) = (\rho_2 - \rho_1)[\langle X \rangle|_0 - (\langle X \rangle|_0)^2]^{1/2}, \quad (7.13)$$

such that, $A_e = A$ (assuming $\langle X \rangle|_0 = 1/2$). The sensitivity of \dot{h} to A_e (7.9) suggests that the growth rate for immiscible fluids will exceed that of miscible fluids at the same Atwood number and acceleration (assuming that the other empirical constants do not change substantially). This could explain why experiments with immiscible fluids (Read 1984; Dimonte & Schneider 2000) and simulations employing front tracking (Glimm *et al.* 2001) appear to exhibit faster growth rates than cases with species diffusion (Dimonte *et al.* 2004).

8. Conclusions

We have developed a large-eddy simulation methodology well-suited for large-scale simulations of Rayleigh–Taylor instability. The method converges to DNS at low Reynolds numbers, while allowing for stable solutions at high (effective) Reynolds numbers. We used the method to perform an LES of RTI at a grid resolution of 1152^3 points. The simulated flow appears to progress through four stages, including a mixing transition. The mixing transition is evident in the evolution of the mole-fraction p.d.f., which indicates an increase in mixed fluid for $6 < h/\lambda_o < 15$. The increase in the mixing rate coincides with formation of an inertial range in the two-dimensional spectrum of vertical velocity. During this stage, the growth rate of the mixing layer is somewhat suppressed. Hence, attempts to measure α for $h/\lambda_0 < 15$ are likely to yield erroneous results.

The flow develops broad power-law ranges in both the density and vertical velocity spectra by late time. The spectra for horizontal velocity components appear to lag the vertical velocity spectrum in development, matching first at higher wavenumbers where eddy turnover times are short. Well-defined peaks in the energy spectra at

low wavenumbers and the collapse of mole-fraction averages scaled by mixing height indicate that the flow is well resolved and the growth statistics are well converged for the duration of the simulation.

We have derived a relationship between growth and mixing rates that approximates the LES data. The relation is based on an observed correlation between a mix-dependent Atwood number and the net mass flux through the ($z=0$)-plane. The relation suggests faster growth for immiscible fluids than for miscible fluids.

Finally, we emphasize that realization of self-similar growth requires $\lambda_o \ll \lambda \ll L$. These conditions must be satisfied for growth to be independent of both initial conditions and boundary conditions. By measuring growth of certain variables in units of λ_o , we documented progress of the flow towards its asymptotic state. By $h/\lambda_o = 30$, many variables appear to have reached their asymptotic limit; however, there is still no appreciable inertial range in the secondary flow spectra (u and v) and the kinetic to potential energy ratio is still gradually increasing. Larger simulations, reaching higher values of h/λ_o , are needed to investigate whether the growth rate ever becomes independent of Reynolds number.

We express thanks to Professor P. E. Dimotakis for sharing his valuable insights into this flow, including the effects of mixing on the growth rate. This work was performed under the auspices of the US Department of Energy by the University of California Lawrence Livermore National Laboratory under contract no. W-7405-Eng-48.

Appendix A. Numerics

A.1. Combination of species transport equations

The mass fractions satisfy

$$Y_1(\mathbf{x}, t) + Y_2(\mathbf{x}, t) = 1 \quad (\text{A } 1)$$

and with ρ_1 and ρ_2 denoting the constant densities of the light and heavy fluids, respectively, the specific volume satisfies

$$\frac{1}{\rho(\mathbf{x}, t)} = \frac{Y_1(\mathbf{x}, t)}{\rho_1} + \frac{Y_2(\mathbf{x}, t)}{\rho_2}. \quad (\text{A } 2)$$

Equations (2.1), (A 1) and (A 2) can be used to derive the following divergence relation for miscible fluids (Joseph 1990)

$$\frac{\partial u_j}{\partial x_j} = -\frac{\partial}{\partial x_j} \left(\frac{D}{\rho} \frac{\partial \rho}{\partial x_j} \right). \quad (\text{A } 3)$$

Hence, for incompressible mixing of unequal-density fluids, a convenient equation for ρ is

$$\frac{\partial \rho}{\partial t} + u_j \frac{\partial \rho}{\partial x_j} = \rho \frac{\partial}{\partial x_j} \left(\frac{D}{\rho} \frac{\partial \rho}{\partial x_j} \right), \quad (\text{A } 4)$$

which replaces (2.10) in the governing set of equations and is solved in the LES manner by replacing D with D_T .

A.2. Spatial differencing

Spatial derivatives are computed in the code with the following tenth-order compact scheme

$$\begin{aligned} \beta f'_{j-2} + \alpha f'_{j-1} + f'_j + \alpha f'_{j+1} + \beta f'_{j+2} \\ = c \frac{f_{j+3} - f_{j-3}}{6\Delta_i} + b \frac{f_{j+2} - f_{j-2}}{4\Delta_i} + a \frac{f_{j+1} - f_{j-1}}{2\Delta_i}, \end{aligned} \quad (\text{A } 5)$$

$$\alpha = \frac{1}{2}, \quad \beta = \frac{1}{20}, \quad a = \frac{17}{12}, \quad b = \frac{101}{150}, \quad c = \frac{1}{100},$$

where j is a grid index along a line with N points in the i direction, and Δ_i is the grid spacing in that direction. Near the boundaries, the stencil is telescoped in a conservative manner, such that only the boundary nodes contribute to the boundary fluxes (Lele 1992); i.e. at $j=4$ and $j=N-3$

$$\alpha = \frac{4.63271875}{9.38146875}, \quad \beta = \frac{0.451390625}{9.38146875},$$

$$a = 2 \frac{6.66984375}{9.38146875}, \quad b = 4 \frac{1.53}{9.38146875}, \quad c = 6 \frac{0.015}{9.38146875};$$

at $j=3$ and $j=N-2$

$$\alpha = \frac{4.743}{10.67175}, \quad \beta = \frac{0.2964375}{10.67175},$$

$$a = 2 \frac{7.905}{10.67175}, \quad b = 4 \frac{1.23515625}{10.67175}, \quad c = 0;$$

at $j=2$ and $j=N-1$

$$\alpha = \frac{1}{4}, \quad \beta = 0, \quad a = \frac{3}{2}, \quad b = 0, \quad c = 0;$$

and at the boundary nodes

$$f'_1 + 2f'_2 = \left(-\frac{5}{2}f_1 + 2f_2 + \frac{1}{2}f_3 \right) / \Delta_i,$$

$$f'_N + 2f'_{N-1} = \left(\frac{5}{2}f_N - 2f_{N-1} - \frac{1}{2}f_{N-2} \right) / \Delta_i.$$

A.3. Temporal integration

The solution is marched forward in time via the following third-order, variable-time-step predictor–corrector method. For equations of the form

$$\dot{\phi} = F(\phi), \quad (\text{A } 6)$$

the predictor step is

$$\phi^* = \phi^n + \Delta t_{new} [(1 + \mathcal{R})F(\phi^n) - \mathcal{R}F(\phi^{n-1})] \quad (\text{A } 7)$$

and the corrector step is

$$\phi^{n+1} = \phi^* + \Delta t_{new} [\mathcal{A}F(\phi^*) + (\mathcal{B} - \mathcal{R} - 1)F(\phi^n) + (\mathcal{C} + \mathcal{R})F(\phi^{n-1})], \quad (\text{A } 8)$$

where

$$\begin{aligned}\mathcal{R} &= \Delta t_{new}/(2\Delta t_{old}), \\ \mathcal{A} &= (2\Delta t_{new} + 3\Delta t_{old})/[6(\Delta t_{new} + \Delta t_{old})], \\ \mathcal{B} &= (\Delta t_{new} + 3\Delta t_{old})/(6\Delta t_{old}), \\ \mathcal{C} &= -\Delta t_{new}^2/[6\Delta t_{old}(\Delta t_{new} + \Delta t_{old})],\end{aligned}$$

with Δt_{old} denoting the time increment between the $n-1$ and n time steps, and Δt_{new} being the time increment between the n and $n+1$ times.

The density equation (A 4) is integrated by straightforward application of the predictor–corrector scheme. However, it must be advanced in conjunction with the momentum equation, which requires each step to be further broken down according to the following pressure-projection algorithm. The pressure-projection scheme for the momentum equation is derived by integrating (2.11) from t to $t + \Delta t$, i.e.

$$(\rho u_i)^{n+1} = (\rho u_i)^n + \int_t^{t+\Delta t} \Lambda_i dt + \Delta t \left(\rho_a g_i - \frac{\partial p_a}{\partial x_i} \right), \quad (\text{A } 9)$$

where (μ is replaced by μ_T in the expression for τ_{ij})

$$\begin{aligned}\Lambda_i &\equiv \frac{\partial}{\partial x_j} (\tau_{ij} - \rho u_i u_j), \\ p_a &\equiv \frac{1}{\Delta t} \int_t^{t+\Delta t} p dt, \\ \rho_a &\equiv \frac{1}{\Delta t} \int_t^{t+\Delta t} \rho dt \approx \frac{1}{2}(\rho^{n+1} + \rho^n).\end{aligned}$$

Equation (A 9) is now split into two parts. The first part accounts for advection and diffusion, i.e.

$$\Phi_i = (\rho u_i)^n + \int_t^{t+\Delta t} \Lambda_i dt, \quad (\text{A } 10)$$

while the second part accounts for pressure and acceleration, i.e.

$$(\rho u_i)^{n+1} = \Phi_i + \Delta t \left(\rho_a g_i - \frac{\partial p_a}{\partial x_i} \right). \quad (\text{A } 11)$$

The integral in (A 10) is approximated by the predictor formula

$$\int_t^{t+\Delta t} \Lambda_i dt \approx \Delta t_{new} [(1 + \mathcal{R}) \Lambda_i^n - \mathcal{R} \Lambda_i^{n-1}].$$

At this point, p_a is needed in order to advance (A 11). Taking the divergence of (A 11) results in the Poisson equation

$$\frac{\partial^2 p_a}{\partial x_i^2} = \frac{1}{\Delta t} \left[\frac{\partial}{\partial x_i} \Phi_i - \frac{\partial}{\partial x_i} (\rho u_i)^{n+1} \right] + \frac{\partial}{\partial x_i} (\rho_a g_i). \quad (\text{A } 12)$$

Since $(\rho u_i)^{n+1}$ is unknown at this point, an approximation is used, whereby $\partial(\rho u_i)^{n+1}/\partial x_i$ is expanded and combined with (A 3) to obtain

$$\frac{\partial}{\partial x_i} (\rho u_i)^{n+1} = u_i^{n+1} \frac{\partial \rho^{n+1}}{\partial x_i} - \rho^{n+1} \frac{\partial}{\partial x_i} \left(\frac{D_T}{\rho^{n+1}} \frac{\partial \rho^{n+1}}{\partial x_i} \right).$$

The right-hand side is evaluated by extrapolating u_i^{n+1} from previous timesteps, i.e.

$$u_i^{n+1} = u_i^n + (u_i^n - u_i^{n-1}) (\Delta t_{\text{new}} / \Delta t_{\text{old}}) + O(\Delta t^2).$$

In this first step, ρ^* (the predicted value of ρ at $n+1$) is used in place of ρ^{n+1} . With these substitutions, (A 12) is solved for p_a (see Appendix A.4), which is then substituted into (A 11) to compute $(\rho u_i)^*$.

In the corrector step, ρ^{n+1} is first obtained from (A 8). With predicted values (asterisks) now available at the $n+1$ time, the trapezoidal rule can be used for the integral in (A 10), i.e.

$$\int_t^{t+\Delta t} \Lambda_i \, dt = \frac{1}{2} \Delta t [\Lambda_i^* + \Lambda_i^n] + O(\Delta t^3).$$

In this second step, (A 12) is solved using $(\rho u_i)^*$ in place of $(\rho u_i)^{n+1}$. No approximation is necessary for ρ^{n+1} since this is now known. Finally, (A 11) is used to compute $(\rho u_i)^{n+1}$, from which u_i^{n+1} is obtained.

A.4. Poisson solver

With periodic boundary conditions in x and y , the Poisson equation can be Fourier transformed to obtain

$$\mathcal{F}_{xy} \left\{ \frac{\partial^2 p}{\partial x^2} + \frac{\partial^2 p}{\partial y^2} + \frac{\partial^2 p}{\partial z^2} \right\} = \Omega(x, y, z) \Rightarrow -k_x^2 \hat{p} - k_y^2 \hat{p} + \hat{p}'' = \hat{\Omega}(k_x, k_y, z),$$

where $\hat{p}'' = \partial^2 \hat{p} / \partial z^2$. Thus (j is the z -index of the grid)

$$\hat{p}_j'' = \hat{\Omega}_j + k^2 \hat{p}_j \quad \text{with } k^2 = k_x^2 + k_y^2. \quad (\text{A 13})$$

An eighth-order, compact approximation for \hat{p}_j'' can be written as (Collatz 1966; Lele 1992)

$$\beta \hat{p}_{j-2}'' + \alpha \hat{p}_{j-1}'' + \hat{p}_j'' + \alpha \hat{p}_{j+1}'' + \beta \hat{p}_{j+2}'' = b \frac{\hat{p}_{j+2} - 2\hat{p}_j + \hat{p}_{j-2}}{4\Delta z^2} + a \frac{\hat{p}_{j+1} - 2\hat{p}_j + \hat{p}_{j-1}}{\Delta z^2}, \quad (\text{A 14})$$

where $\alpha = 344/1179$, $\beta = 23/2358$, $a = 320/393$ and $b = 310/393$. Inserting (A 13) into (A 14), and collecting the coefficients of \hat{p}_j yields the linear system

$$\begin{aligned} & \left[\beta k^2 - \frac{b}{4\Delta z^2} \right] \hat{p}_{j-2} + \left[\alpha k^2 - \frac{a}{\Delta z^2} \right] \hat{p}_{j-1} + \left[k^2 + \frac{b}{2\Delta z^2} + \frac{2a}{\Delta z^2} \right] \hat{p}_j \\ & + \left[\alpha k^2 - \frac{a}{\Delta z^2} \right] \hat{p}_{j+1} + \left[\beta k^2 - \frac{b}{4\Delta z^2} \right] \hat{p}_{j+2} \\ & = - \left[\beta \hat{\Omega}_{j-2} + \alpha \hat{\Omega}_{j-1} + \hat{\Omega}_j + \alpha \hat{\Omega}_{j+1} + \beta \hat{\Omega}_{j+2} \right]. \end{aligned} \quad (\text{A 15})$$

At points neighbouring boundaries ($j=2$ and $j=N-1$) a fourth-order, compact stencil is used, in which $\alpha=1/10$, $\beta=0$, $a=6/5$ and $b=0$. Neumann boundary conditions are implemented at $j=1$ and $j=N$ via the second-order approximations:

$$\frac{3}{2\Delta z} \hat{p}_1 - \frac{2}{\Delta z} \hat{p}_2 + \frac{1}{2\Delta z} \hat{p}_3 = -\hat{p}'_1, \quad (\text{A 16})$$

$$-\frac{1}{2\Delta z} \hat{p}_{N-2} + \frac{2}{\Delta z} \hat{p}_{N-1} - \frac{3}{2\Delta z} \hat{p}_N = -\hat{p}'_N, \quad (\text{A 17})$$

where \hat{p}'_1 and \hat{p}'_N are the $x - y$ transforms of the z -derivatives at the walls. The simplest boundary condition for p is the inviscid hydrostatic gradient, $p' = \rho g_z$.

The pentadiagonal matrix associated with (A 15)–(A 17) is well-conditioned except for $k = 0$, in which case it is singular. This situation arises because, with Neumann conditions at both ends of the domain, the solution for the pressure is non-unique, i.e. the pressure is only defined within a constant. The constant is specified by replacing any one of the $k = 0$ equations in (A 15) by $\hat{p}_j(k=0) = \text{constant}$. This fixes the mean pressure on the chosen z -plane, which in turn, sets the mean pressure for the entire domain. This condition should be applied near the centre of the domain, e.g. at $j = N/2$, rather than at the boundaries, because loss of (A 16) or (A 17) at $k = 0$ can lead to drift in the mean wall-normal derivative at that boundary. Note that the value of the constant is irrelevant since the governing equations depend only on ∇p .

Appendix B. Filtering

In the simulations, the LES filter is applied explicitly to ρ and ρu_i after each complete time step; this is done in order to reduce aliasing errors. The following eighth-order compact filter is chosen for its spectral-like properties in preserving low and moderate wavenumbers (Lele 1992),

$$\begin{aligned} \beta \bar{f}_{j-2} + \alpha \bar{f}_{j-1} + \bar{f}_j + \alpha \bar{f}_{j+1} + \beta \bar{f}_{j+2} &= af_j + \frac{1}{2}b(f_{j-1} + f_{j+1}) \\ &+ \frac{1}{2}c(f_{j-2} + f_{j+2}) + \frac{1}{2}d(f_{j-3} + f_{j+3}) + \frac{1}{2}e(f_{j-4} + f_{j+4}), \end{aligned} \quad (\text{B } 1)$$

where j is a grid index and

$$\alpha = 0.61, \quad \beta = 0.195, \quad a = 0.953515625, \quad b = 1.294375, \quad (\text{B } 2)$$

$$c = 0.3528125, \quad d = 0.010625, \quad e = -0.001328125. \quad (\text{B } 3)$$

The filter is applied sequentially in each direction. The transfer function associated with this filter is depicted in figure 22. Also displayed is the implicit filter associated with the tenth-order compact differencing scheme, used to compute spatial derivatives. Comparing the transfer functions of the implicit and explicit filters, it is clear that the wavenumbers remaining after application of the explicit filter are resolved well by the differencing scheme. Both of these filters are non-monotonic in physical space; hence, they produce Gibbs oscillations whenever the Fourier series representation of the flow contains terms above the filter cut-off. Gibbs oscillations are not errors; they are simply a consequence of convolving a high-resolution (low-wavenumber-preserving) filter kernel with a broadbanded function. Nevertheless, for practical reasons, it is desirable to remove these oscillations from the numerical solution in order to ensure that variables remain within their original bounds, e.g. $0 \leq Y_m \leq 1$; this is accomplished with the subgrid-scale models discussed in § 2.3.

Rapid oscillations in the subgrid-scale viscosity coefficient μ_T are smoothed with the Gaussian filter

$$\begin{aligned} \overline{\bar{f}}_j &= \frac{3565}{10368} f_j + \frac{3091}{12960}(f_{j-1} + f_{j+1}) + \frac{1997}{25920}(f_{j-2} + f_{j+2}) \\ &+ \frac{149}{12960}(f_{j-3} + f_{j+3}) + \frac{107}{103680}(f_{j-4} + f_{j+4}), \end{aligned} \quad (\text{B } 4)$$

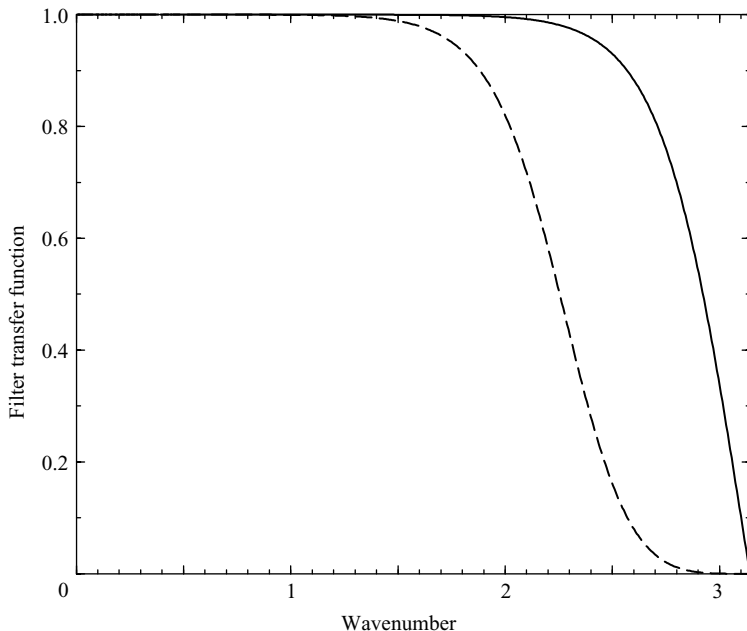


FIGURE 22. Transfer functions for implicit and explicit filters. —, implicit filter of tenth-order compact finite-difference scheme; ---, eighth-order LES filter explicitly applied to ρ and ρu_i , following each time step.

denoted by the double overbar. The filter employed in the subgrid-scale diffusion coefficient D_T , denoted by a triple overbar, is

$$\overline{\overline{\overline{f_j}}} = 0.18733 f_j + 0.15365 (f_{j-1} + f_{j+1}) + 0.12338 (f_{j-2} + f_{j+2}) \\ + 0.096354 (f_{j-3} + f_{j+3}) + 0.032951 (f_{j-4} + f_{j+4}), \quad (B5)$$

which helps to fill in gaps between the over and undershoots.

REFERENCES

- ANUCHINA, N. N., KUCHERENKO, Y. A., NEUVAZHAEV, V. E., OGIBINA, V. N., SHIBARSHOV, L. I. & YAKOVLEV, V. G. 1978 *Izv. Akad. Nauk SSSR Mekh. Zhidk. Gaza* **6**, 157.
- BARONE, M. F. & LELE, S. K. 2002 A numerical technique for trailing edge acoustic scattering problems. *AIAA Paper* 2002-0226, 40th AIAA Aerospace Sciences Meeting and Exhibit.
- CHANDRASEKHAR, S. 1955 The character of the equilibrium of an incompressible heavy viscous fluid of variable density. *Proc. Camb. Phil. Soc.* **51**, 162–178.
- CLARK, T. T. 2003 A numerical study of the statistics of a two-dimensional Rayleigh–Taylor mixing layer. *Phys. Fluids* **15**, 2413–2423.
- COLLATZ, L. 1966 *The Numerical Treatment of Differential Equations*. Springer.
- COOK, A. W. & CABOT, W. H. 2004 A high-wavenumber viscosity for high-resolution numerical methods. *J. Comput. Phys.* **195**, 594–601.
- COOK, A. W. & DIMOTAKIS, P. E. 2001 Transition stages of Rayleigh–Taylor instability between miscible fluids. *J. Fluid Mech.* **443**, 69–99.
- COOK, A. W. & ZHOU, Y. 2002 Energy transfer in Rayleigh–Taylor instability. *Phys. Rev. E* **66**, 026312.
- DALZIEL, S. B., LINDEN, P. F. & YOUNGS, D. L. 1999 Self-similarity and internal structure of turbulence induced by Rayleigh–Taylor instability. *J. Fluid Mech.* **399**, 1–48.

- DIMONTE, G. & SCHNEIDER, M. 2000 Density ratio dependence of Rayleigh–Taylor mixing for sustained and impulsive acceleration histories. *Phys. Fluids* **12**, 304–321.
- DIMONTE, G., YOUNGS, D. L., DIMITS, A. *et al.* 2004 A comparative study of the turbulent Rayleigh–Taylor (RT) instability using high-resolution 3d numerical simulations: The alpha-group collaboration. *Phys. Fluids* **16**, 1668–1693.
- DIMOTAKIS, P. E. 2000 The mixing transition in turbulence. *J. Fluid Mech.* **409**, 69–97.
- DIMOTAKIS, P. E. & MILLER, P. L. 1990 Some consequences of the boundedness of scalar fluctuations. *Phys. Fluids* **2**, 1919–1920.
- DUFF, R. E., HARLOW, F. H. & HIRT, C. W. 1962 Effects of diffusion on interface instability between gases. *Phys. Fluids* **5**, 417–425.
- GLIMM, J., GROVE, J. W., LI, X. L., OH, W. & SHARP, D. H. 2001 A critical analysis of Rayleigh–Taylor growth rates. *J. Comput. Phys.* **169**, 652–677.
- JOSEPH, D. D. 1990 Fluid dynamics of two miscible liquids with diffusion and gradient stresses. *Eur. J. Mech. B/Fluids* **9**, 565–596.
- LELE, S. K. 1992 Compact finite difference schemes with spectral-like resolution. *J. Comput. Phys.* **103**, 16–42.
- LINDEN, P. F., REDONDO, J. M. & YOUNGS, D. L. 1994 Molecular mixing in Rayleigh–Taylor instability. *J. Fluid Mech.* **265**, 97–124.
- MILLER, P. L. & DIMOTAKIS, P. E. 1991 Reynolds number dependence of scalar fluctuations in a high Schmidt number turbulent jet. *Phys. Fluids* **3**, 1156–1163.
- RAMAPRABHU, P. & ANDREWS, M. J. 2004 Experimental investigation of Rayleigh–Taylor mixing at small Atwood numbers. *J. Fluid Mech.* **502**, 233–271.
- RAYLEIGH, LORD 1883 Investigation of the character of the equilibrium of an incompressible heavy fluid of variable density. *Proc. R. Math. Soc.* **14**, 170–177.
- READ, K. I. 1984 Experimental investigation of turbulent mixing by Rayleigh–Taylor instability. *Physica D* **12**, 45–58.
- TAYLOR, G. I. 1950 The instability of liquid surfaces when accelerated in a direction perpendicular to their plane. *Proc. R. Soc. Lond. A* **201**, 192–196.
- YOUNGS, D. L. 1984 Numerical simulation of turbulent mixing by Rayleigh–Taylor instability. *Physica D* **12**, 32–44.
- YOUNGS, D. L. 1991 Three-dimensional numerical simulation of turbulent mixing by Rayleigh–Taylor instability. *Phys. Fluids* **3**, 1312–1320.
- YOUNGS, D. L. 1994 Numerical simulation of mixing by Rayleigh–Taylor and Richtmyer–Meshkov instabilities. *Laser Particle Beams* **12**, 725–750.